Appl Phys B (2011) 105:163–180
DOI 10.1007/s00340-011-4729-3

Applied Physics B
Lasers and Optics

Local photonic modes in periodic or random, dielectric, and lasing media

T. Stollenwerk · R. Frank · A. Lubatsch · O. Zaitsev · S.V. Zhukovsky · D.N. Chigrin · J. Kroha

Received: 11 April 2011 / Revised version: 3 August 2011 / Published online: 16 September 2011

Abstract Numerous nanophotonics applications involve the spatial confinement of the electromagnetic field to a length scale comparable to the optical wavelength, such as in photonic crystal (PhC) cavities or defects or in microlasers. First, we review a recently proposed, novel optimization scheme for the efficient construction of maximally localized photonic Wannier functions to be used as a set of basis functions for the description of localized modes in PhCs. We then analyze bistable lasing and the mode switching dynamics in multimode PhC microlasers and describe a recently developed theory for the confined, spatial intensity correlations (second-order coherence) in homogeneously disordered random lasers. Finally, a systematic diagrammatic expansion for the eigenmode renormalization of microlaser cavities due to the laser nonlinearity is described.

T. Stollenwerk · R. Frank · A. Lubatsch · S.V. Zhukovsky · J. Kroha (✉)
Physikalisches Institut, Universität Bonn, Nussallee 12, 53115 Bonn, Germany
e-mail: kroha@th.physik.uni-bonn.de

O. Zaitsev
Department of Information Display, Kyung Hee University, 1 Hoegi-dong, Dongdaemun-gu, Seoul 130-701, Korea

D.N. Chigrin
Fachbereich E, Hochfrequenz- und Kommunikationstechnologie, Universität Wuppertal, Rainer-Gruenter-Str. 21, 42119 Wuppertal, Germany

Present address:
R. Frank
Institut für Theoretische Festkörperphysik, Karlsruhe Institute of Technology, 76128 Karlsruhe, Germany

Present address:
S.V. Zhukovsky
Department of Physics, University of Toronto, 60 St. George St., Toronto, ON M5S 1A7, Canada

1 Introduction and overview

Spatially confined optical modes play a central role in numerous problems of photonics. Photonic crystal (PhC) applications [1] frequently utilize the photonic bandgap effect together with defect, cavity, or waveguide structures to produce localized defect or cavity modes whose frequency lies in the gap of a PhC. Furthermore, in microlasers the locality of lasing modes is instrumental for overcoming the laser threshold and for providing coherent feedback [2, 3]. These applications call for efficient methods to calculate defect or cavity modes in PhCs and for a detailed understanding of the mode structure and dynamics in complex, microscopic lasing systems. In this article, we review our work regarding these problems.

In Sect. 2, we analyze the optimization process to construct maximally localized Wannier functions (MLWF) as a basis set for the expansion of defect and cavity modes in PhCs. The optimized locality of the Wannier basis functions [4–6] is crucial for keeping the dimension of the function space to be used for the expansion of local eigenmodes minimal, and hence for reducing the numerical effort. The commonly used optimization criterion, minimization of the second moment of the Wannier function modulus squared, turns out to have multiple local extrema as a functional of the Wannier function, which hampers finding the optimal one. Our analysis suggests the origin of this unwanted multiplicity and leads us to put forward a new optimization criterion, maximization of the modulus squared integrated over a Wigner–Seitz cell around a given Wannier center [7]. It exhibits a unique, global optimum. We also propose a novel, analytical ansatz for the Wannier function as an initial form that speeds up local optimization procedures, like the commonly used conjugate gradient methods.

Sections 3 to 5 are devoted to lasing systems, where Sect. 3 deals with the dynamics in PhC microresonators with

predefined mode structure, while in Sects. 4 and 5 more general, disordered or chaotic laser systems are treated, respectively. In Sect. 3, the mode competition and the possibility of bistable lasing in multimode microlaser cavities is investigated. We map out the stability diagram of a two-mode microlaser [8, 9] by solving a multimode representation of the semiclassical Maxwell–Bloch equations and show by direct, numerical finite difference time domain (FDTD) calculations [10] that the different lasing modes may be addressed by appropriate seeding pulses [11, 12] and ultrafast switching between the modes is possible [8, 13]. The latter suggests a possible use of such multimode microlasers as microscopic, switchable, multifrequency light sources, as optical storage devices, or for optical pattern recognition.

In Sect. 4, we develop an analytic theory for 3-dimensional, homogeneous random lasers [14], i.e., strongly disordered, laser-active media where the light propagation is diffusive and the lasing modes are not predefined because of the absence of a resonator. In particular, we explain the experimentally observed fact that coherent feedback is possible in homogeneous random lasers although localized eigenmodes due to Anderson localization [15] do not exist. To that end, we show that in the presence of stimulated emission causality [16] implies that the intensity-intensity correlations (second-order coherence) have a finite correlation length ξ, even though the electromagnetic field distribution is extended [17]. We calculate ξ in dependence of the pump rate by solving the diffusive intensity transport theory (including wave interference effects), coupled to the semiclassical laser rate equations [17–19].

Section 5 addresses systems where the resonance frequencies of the lasing modes in the lasing state are strongly renormalized with respect to the passive eigenmodes. These renormalizations have been recognized to be induced by a spatially nonuniform dielectric constant or population inversion [20, 21], typically caused by a nonuniform intensity profile of the lasing mode, or by the nonlinearity of the lasing medium [22, 23]. A systematic, diagrammatic perturbation theory, which allows to calculate corrections to physical quantities to arbitrary order in the laser nonlinearity, has been developed in [24] and applied to gas lasers with chaotic cavities in [25].

2 Efficient construction of Wannier functions

2.1 Formulation of the problem

An efficient way of computing the electromagnetic field distribution of light in a photonic system is to expand the field in terms of an appropriate orthonormal set of basis functions which renders the stationary electromagnetic wave equation as a discrete matrix eigenvalue problem [26]. The proper choice of the set of basis functions is crucial in order to obtain an accurate description while keeping the dimension of the eigenvalue problem minimal. We consider two-dimensional (2D) PhCs, characterized by a periodic dielectric function $\epsilon(\mathbf{r}) = \epsilon(\mathbf{r}+\mathbf{R})$, $\forall \mathbf{R} \in \mathcal{L}$, with $\mathbf{r} = (x, y)$ denoting a 2D vector in the x–y-plane and $\mathbf{R}$ being a lattice vector of some 2D lattice $\mathcal{L}$. The wave equation for time harmonic TM (transverse magnetic), $E(\mathbf{r}, t) = e^{-i\omega t} E(\mathbf{r})$, and TE (transverse electric), $H(\mathbf{r}, t) = \mathrm{e}^{-\mathrm{i}\omega t} H(\mathbf{r})$, polarization reads, respectively,

$$\mathcal{L}_E E(\mathbf{r}) = -\frac{1}{\epsilon(\mathbf{r})}\nabla^2 E(\mathbf{r}) = \frac{\omega^2}{c^2} E(\mathbf{r}), \tag{1}$$

$$\mathcal{L}_H H(\mathbf{r}) = -\nabla \frac{1}{\epsilon(\mathbf{r})}\nabla H(\mathbf{r}) = \frac{\omega^2}{c^2} H(\mathbf{r}). \tag{2}$$

The wave operators $\mathcal{L}_E$ and $\mathcal{L}_H$ are hermitian with respect to the corresponding inner products:

$$\langle f|g\rangle_E = \int_V d^2r\, f^*(\mathbf{r})\epsilon(\mathbf{r})g(\mathbf{r}), \tag{3}$$

$$\langle f|g\rangle_H = \int_V d^2r f^*(\mathbf{r})g(\mathbf{r}). \tag{4}$$

V is the 2D volume of the crystal.

While for propagating wave problems an expansion in terms of Bloch functions, the eigenmodes of the unperturbed PhC, is appropriate [27, 28], for the description of defect, cavity, and also of waveguide structures the use of Wannier functions as a basis set [29–32] is in principle superior, because Wannier functions may be constructed as being localized in space and are still an exact representation of the point symmetry group of the host PhC. Wannier function expansions developed for electronic systems [33, 34] have only recently been applied to the electromagnetic case [4, 35]. Since then, the theory of photonic Wannier functions has been applied to the analysis of 2D PhC cavities, waveguides [35, 36], waveguide crossings [5], and PhC heterostructures [37]. The generalization of the approach to the case of 2D slab PhCs and 3D PhCs has been also reported in [6, 38].

The Bloch functions are the solutions of the wave equations (1) or (2), respectively, in a periodic medium,

$$\mathbf{B}_{n\mathbf{k}}(\mathbf{r}) = e^{i\phi_{n\mathbf{k}}} e^{i\mathbf{kr}} \mathbf{u}_{n\mathbf{k}}(\mathbf{r}) =: e^{i\Phi_{n\mathbf{k}}} \tilde{\mathbf{B}}_{n\mathbf{k}}(\mathbf{r}), \tag{5}$$

where $\mathbf{u}_{n\mathbf{k}}(\mathbf{r})$ is a lattice-periodic envelope function and n is the band index. We have explicitly denoted the arbitrary phase $\phi_{n\mathbf{k}}$ of the Bloch function, the so-called Bloch phase. The Wannier functions are defined as the Fourier transform of the Bloch modes with respect to the wave vector $\mathbf{k}$,

$$\mathbf{W}_{n\mathbf{R}}(\mathbf{r}) = \sum_m U_{nm} \frac{1}{\sqrt{N}} \sum_{\mathbf{k}\in BZ} e^{-i\mathbf{kR}} \mathbf{B}_{m\mathbf{k}}(\mathbf{r}), \tag{6}$$

where, in addition, mixing of different bands may be effected by the unitary matrix U_{nm} [5, 6].

As seen from (5), (6), the Wannier functions involve the undetermined parameters $\phi_{n\mathbf{k}}$ and U_{nm}. For simplicity, band mixing will not be considered further in the present work, i.e., $U_{nm} = \delta_{nm}$. While for arbitrary $\phi_{n\mathbf{k}}$ (and in the more general case also U_{nm}) the Wannier functions are generically not localized in space, these parameters may be adjusted to optimize the locality. This constitutes a complex, high-dimensional optimization problem [39]; the dimension given by the number of Bloch functions used. It is, therefore, crucial to have an optimization procedure which efficiently and at the same time reliably converges to the optimally localized Wannier function.

In the following, we analyze the optimization process with respect to two different locality criteria, (i) the commonly used second moment (SM) criterion [4, 6, 40], and (ii) the new integrated moment (IM) criterion, which maximizes the modulus squared of the Wannier function within a Wigner–Seitz cell around the Wannier function center [7]. For each criterion, we compare the results of the conjugate gradient (CG) algorithm (which is fast in finding an extremum, but only local) with the results of a numerically more costly but global genetic optimization algorithm (GA) [41] as a benchmark. Taking the biologic evolution in nature as a model, the GA method works with a population of individuals which pass through a selection procedure and can reproduce themselves. Each Wannier function represents an individual. The set of Bloch phases, which determines the Wannier function, is represented as a large, binary string. The GA method starts with a population of random Wannier functions and passes them through a selection procedure where only that one half of the Wannier functions are retained which are most strongly localized with respect to the given locality criterion ("most fit individuals"). In a second step, these survived individuals are allowed to reproduce themselves by randomly mixing their strings of phases, thus passing their attributes to the offsprings. Together with their off-springs, the survived individuals, which correspond to better localized Wannier functions, comprise the new generation. By iterating this procedure over several thousands of generations the algorithm will converge slowly but definitely towards the global extremum. Once the GA procedure has reached the valley of the global extremum, the CG method is applied subsequently to the GA algorithm in order to accelerate the convergence and improve the accuracy of the solution [41].

Four different two-dimensional photonic crystals have been considered for both fundamental polarizations. Square (Sq) and triangular (Tr) lattices of dielectric rods in air (D) and air rods in dielectric (A) are considered. In what follows, we will refer to these systems as Sq–D, Tr–D, Sq–A, and Tr–A, respectively. The radius of rods and the dielectric constant of dielectric material and air are chosen to be $r_0/a = 0.2$, $\epsilon = 12$, and $\epsilon = 1$, respectively.

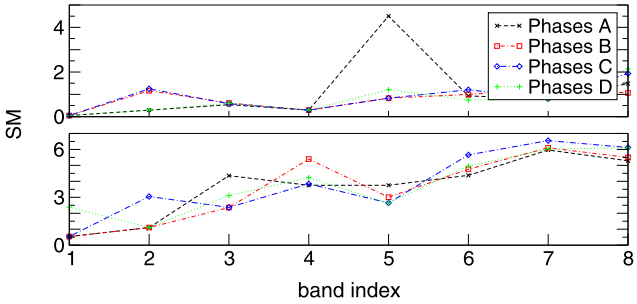

Fig. 1 Second moments $\mathcal{S}_n$ (inverse locality) of the Wannier functions in the nth band, minimized by using the conjugate gradient method [7]. Four different, randomly chosen initial sets of Bloch phases, A, B, C, D, were used for the CG optimization. *Top*: Sq–D crystal, TM polarization. *Bottom*: Tr–D crystal, TE polarization

2.2 Second moment optimization

The second moment of the Wannier function $W_{n\mathbf{R}}(\mathbf{r})$ is defined as

$$\mathcal{S}_n\big(\{\phi_{n\mathbf{k}}\}\big) = \big\langle W_{n\mathbf{R}}|(\mathbf{r}-\mathbf{r}_0)^2|W_{n\mathbf{R}}\big\rangle_{E/H}, \tag{7}$$

with $\mathbf{r}_0$ being the Wannier center. Two positions of the Wannier center have been considered, (i) in the center of the scatterer ("on-site") and (ii) in the geometrical center between four (three) scatterers in the case of square (triangular) lattices ("between").

The SM, (7), exhibits multiple extrema as a functional of the Wannier function, i.e., depending on the Bloch phases. This follows from the fact that the extremum found by the local GC method depends sensitively on the initial set of Bloch phases used as a starting point of the optimization. As a representative example, the SM (i.e., inverse locality) of the SM-optimized Wannier functions, minimized by the GC method, is shown in Fig. 1 for four different, random sets of the initial Bloch phases for Sq–D (TM polarization, upper panel) and for Tr–D (TE polarization, lower panel) structures, respectively. The sensitivity to the initial set of Bloch phases is clearly seen.

In Fig. 2, the evolution of the GA results is depicted for two representative systems and polarizations. Every 100 generations, a Wannier function with highest locality in the current population was taken as a starting point for the subsequent CG optimization. Over the first several thousand generations, the locality of the resulting Wannier functions is varying strongly, indicating hopping of the solution among different local minima due to the stochastic nature of the algorithm. At the top panel of Fig. 2, one can observe how the algorithm is stuck in a local minimum over several thousands of generations, before it escapes and reaches

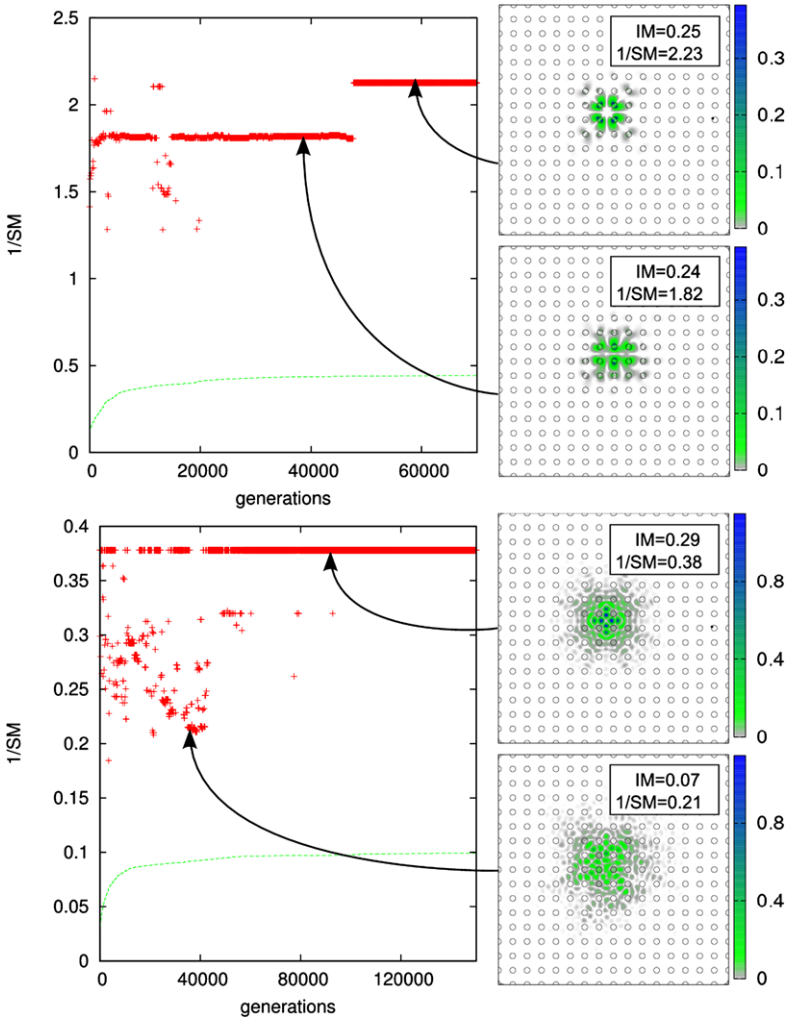

Fig. 2 Locality ($1/\mathcal{S}_n$) of the SM-optimized Wannier functions as a function of GA generation for the Sq–D structure, TM polarization, 3rd band (*top*) and for the Sq–A structure, TE polarization, 5th band (*bottom*) [7]. The *dashed*, *green line* shows the locality of the best-localized Wannier function in each generation. Every 100 generations, these Wannier functions served as a starting point for the subsequent CG optimization step (*red crosses*). On the *right-hand side*, the modulus square of the SM-optimized Wannier function is shown for an early (*top*: 40,000th, *bottom*: 38,300th) and a later (*top*: 60,000th, *bottom*: 100,000th) generation, respectively

the global minimum valley at around the 50,000th generation. An improvement of the locality for later generations is clearly seen from the modulus square of the optimized Wannier functions (Fig. 2, right panels). Despite the multiple local minima, the discontinuous nature of the GA method ensures with stochastic certainty that the global minimum of the SM is found, providing the best localization of the Wannier functions with respect to a given locality measure. At the same time, however, the numerical load of the GA method exceeds the one of the CG method by far, making it inappropriate for routine application for an efficient construction of maximally localized Wannier functions.

2.3 Integrated modulus optimization

The complicated structure of the Wannier functions at large distances, which is expressed by several local minima of their SMs and the associated difficulties in the construction of maximally localized Wannier functions, motivates the search for a simpler criterion for the locality of Wannier functions. Therefore, the integrated modulus square (IM)

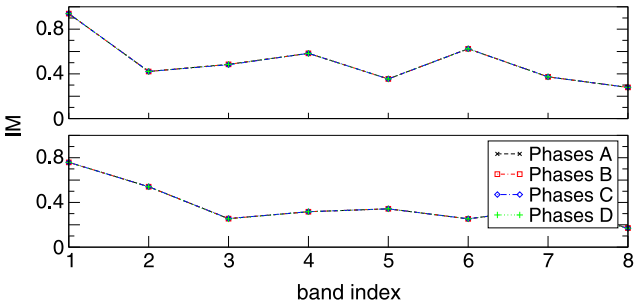

Fig. 3 Locality ($\mathcal{I}_n$) of the Wannier functions optimized with respect to the IM locality measure using the CG method. Four different randomly chosen initial sets of Bloch phases were used for the CG optimization. *Top*: Sq–D crystal, TM polarization. *Bottom*: Tr–D crystal, TE polarization

criterion has been introduced [7]. It is defined as

$$\mathcal{I}_n\left(\{\phi_{n\mathbf{k}}\}\right) = \int_{UC} d^2r \mathbf{W}^*_{n\mathbf{R}}(\mathbf{r}) X(\mathbf{r}) \mathbf{W}_{n\mathbf{R}}(\mathbf{r}), \tag{8}$$

where the integration region is the first Wigner–Seitz unit cell around the Wannier center. We choose the function $X(\mathbf{r})$

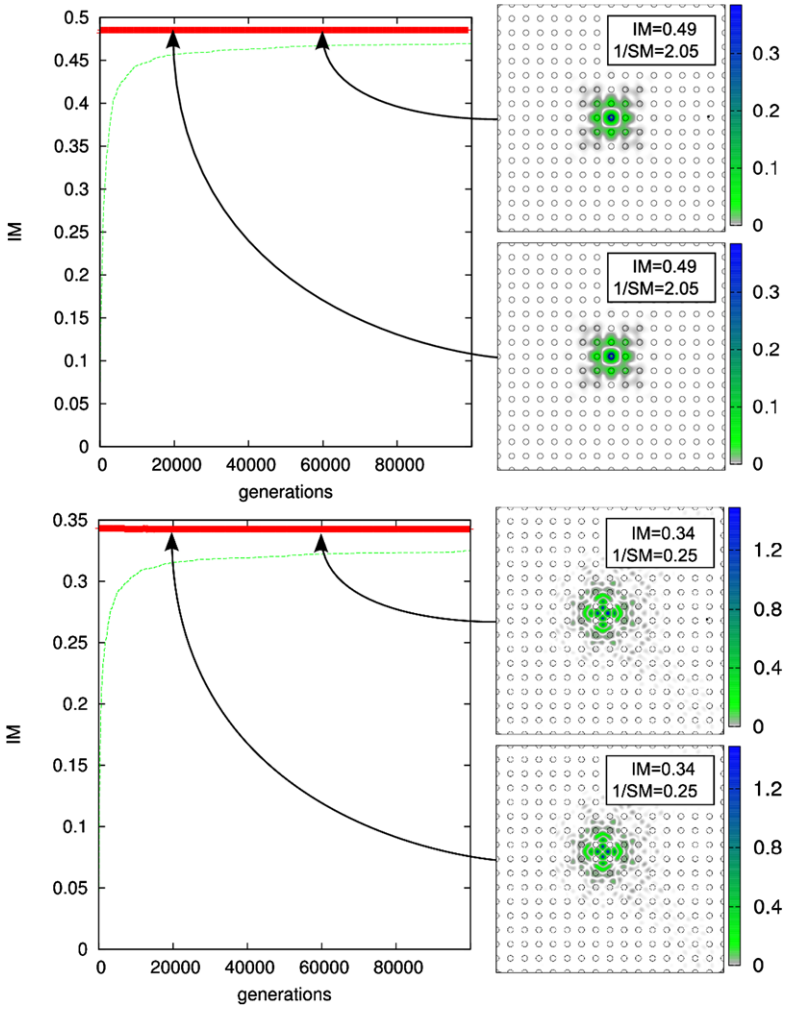

Fig. 4 Locality ($\mathcal{I}_n$) of the IM-optimized Wannier functions as a function of GA generation for the Sq–D structure, TM polarization, 3rd band (*top*) and for the Sq–A structure, TE polarization, 5th band (*bottom*). The dashed green line shows the locality of the best-localized Wannier function in each generation. Every 100 generations, these Wannier functions served as a starting point for the subsequent CG optimization step (*red crosses*). On the *right-hand side*, the modulus square of the IM-optimized Wannier functions is shown for an early (20,000th) and a later (60,000) generation, respectively

in such a way, that the IM is equal to unity for a Wannier function which is completely confined within such a unit cell. i.e.,

$$X(\mathbf{r}) = \begin{cases} \epsilon(\mathbf{r}) & \text{for TM,} \\ 1 & \text{for TE.} \end{cases} \tag{9}$$

A well localized Wannier function corresponds to a large IM, and one needs to maximize the IM in order to obtain the maximally localized Wannier functions. The IM is a rather strict criterion, since it does not depend on the structure of the Wannier functions outside of the integration region. Note that it may be generalized straightforwardly to integrations over a larger volume around the Wannier center, in case satisfactory localization within the first Wigner–Seitz cell is not possible.

We examined the IM locality measure as a localization criterion for the same four different physical systems and both polarizations as it was done in the SM case. First, we show in Fig. 3 the maximized IM for Wannier functions with different band indices n, using the same four different, randomly chosen initial sets of Bloch phases as in Sect. 2.2. In contrast to the SM case, the localities of the resulting Wannier functions coincide for all four sets of phases. This is the case for all considered systems and polarizations. It indicates strongly that the IM locality measure possesses a unique, global maximum only.

To support this hypothesis, we applied the GA method to solve the optimization problem. For all considered structures, no significant variation of the locality has been observed for different GA generations. Representative examples are shown in Fig. 4. One can clearly see, that over many thousands of generations the locality of the Wannier functions optimized with respect to the IM criterion stays constant. This provides strong numerical support that the considered optimization problem possesses a single extremum, making the procedure independent of the choice of the initial set of Bloch phases. As a consequence, the use of the IM as a locality criterion together with the CG as an optimization method represents a fast as well as reliable method for the construction of maximally localized Wannier functions. Figures 5 and 6 show the maximally localized Wan-

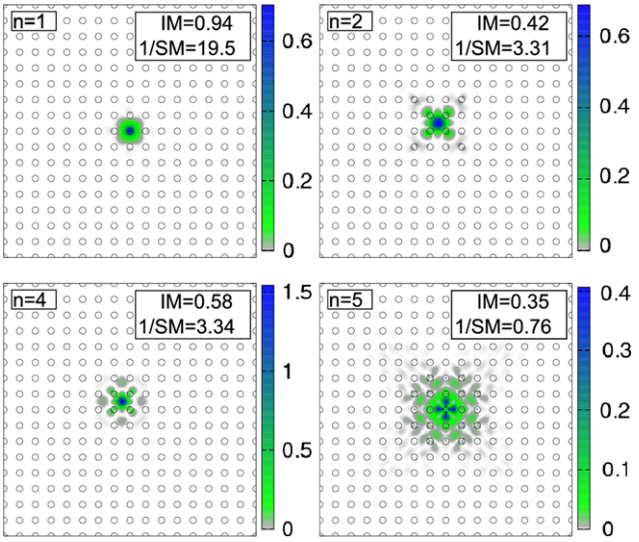

Fig. 5 Modulus square of the maximally localized Wannier functions (with respect to the IM) for the Sq–D structure (TM polarization). The Wannier center was chosen as "on-site" for the 1st and 5th band and as "between" for the 2nd and 4th band

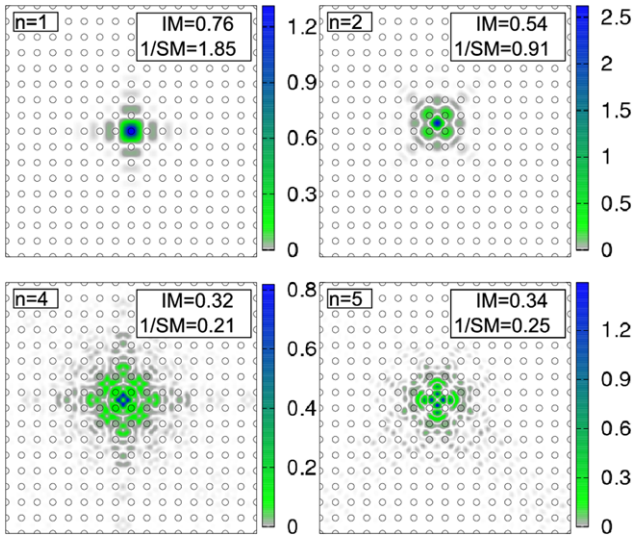

Fig. 6 Modulus square of the maximally localized Wannier functions (with respect to the IM) for Sq–A structure (TE polarization). The Wannier center was chosen as "on-site" for the 1st band and as "between" for the 2nd, 4th, and 5th band

nier functions for the first several bands of the Sq–D (TM polarization) and Sq–A (TE polarization) structures, respectively. In both cases, the IM criterion was used along with the CG method. The optimized Wannier functions demonstrate good locality which degrades slowly with increasing band indices, since the envelope functions become more and more oscillatory, reflecting the not-plane-wave like nature of Bloch modes.

The IM optimization criterion is free of local maxima, simple to evaluate numerically and can be generalized in a straight-forward way to confinement in a volume larger then the first Wigner–Seitz cell, if necessary, e.g., in higher bands. These features have led us to put forward the IM criterion as being superior to the commonly used SM criterion. It is worth noting, that the Wannier functions optimized with respect to the IM and SM criteria are in general not equal, even if the global minimum of the SM or the global maximum of the IM has been reached. For example, for the system of dielectric rods in air (TM polarization), the SM- and IM-optimized Wannier functions coincide for the 1st and the 2nd band (not shown), but not for the third band (top right Wannier function in Figs. 2 and 4). The suitability of the Wannier functions optimized in this way for the calculation of field distributions in PhC cavities has been demonstrated for selected examples in [7].

2.4 Choice of initial conditions

Even though the IM optimization criterion does not show multiple local maxima, as our analysis indicated, a proper choice of the starting set of Bloch phases may greatly facilitate and accelerate the convergence of the optimization. In [7], we have proposed an analytical expression for a generic set of Bloch phases to be used as a starting point for the optimization procedure. It reads

$$\tan(2\phi_{\mathbf{k}}) = \frac{-\int_{UC} d^2r 2\mathrm{Re}(\tilde{B}_{n\mathbf{k}})\mathrm{Im}(\tilde{B}_{n\mathbf{k}})}{\int_{UC} d^2r\{\mathrm{Re}(\tilde{B}_{n\mathbf{k}})^2 - \mathrm{Im}(\tilde{B}_{n\mathbf{k}})^2\}}, \tag{10}$$

where $\tilde{B}_{n\mathbf{k}} = [\tilde{\mathbf{B}}_{n\mathbf{k}}(\mathbf{r}) \cdot \tilde{\mathbf{B}}_{n\mathbf{k}}(\mathbf{r})]^{1/2}$ is the (complex) amplitude of the vector Bloch function. This choice is based on the fact, proven in [7], that the Bloch phases $\phi_{\mathbf{k}}$, (10), solve the Wannier IM optimization problem exactly, if the Wannier functions are real-valued (which can always be achieved by proper choice of the $\phi_{\mathbf{k}}$) and if the real part of all components of the vector Bloch functions have the same sign $\tilde{\mathbf{B}}_{n\mathbf{k}}(\mathbf{r})$ for all space points $\mathbf{r}$ in the unit cell and for all wave vectors $\mathbf{k}$ in the first Brillouin zone.

3 Bistability and ultrafast switching in multimode microlasers

Microlasers with cavity sizes comparable to the light wavelength λ are promising from both fundamental and application points of view [42] for use as integrated coherent light sources. Making microlasers capable of multiple-wavelength emission contributes even more toward miniaturization of optical components, and also provides an additional degree of freedom in light control. The common approach toward microlaser tunability is in essence modification of the optical properties of a single-mode cavity by thermal [43, 44], micromechanical [45, 46], or electrooptical means [47–49].

In contrast, we have proposed the concept of a *switchable microlaser*, comprised of a multimode laser microresonator, where lasing can be switched on demand to any of its eigenmodes [8]. We have shown that a definite resonator mode can be selected for lasing by injection seeding [11, 12, 50, 51], i.e., by injecting an appropriate pulse before and during the onset of lasing, such that the stimulated emission builds up in a chosen mode from this seeding field rather than from the random noise present in the system due to quantum fluctuations and spontaneous emission. We investigate the time needed for switching between different lasing modes and analyze how this process is influenced by noise in competition with the seeding signal [8]. Multistable microlasers with more than two different, stationary lasing states have been investigated in [12].

The semiclassical multimode laser model of [52] has been generalized to study the dynamics of individual modes in a two-mode laser, where an external field is present in the cavity due to the injection seeding. An example of a two-mode microcavity, which we have chosen to study numerically, is depicted in Fig. 7a. The microcavity is based on two coupled defects in a two-dimensional (2D) photonic crystal (PhC) made of dielectric nanopillars [54, 55]. Pillar PhCs are practically feasible by state-of-the-art fabrication technology [56, 57].

The system of two identical coupled single-mode cavities supports two modes, namely the bonding (symmetric) and the antibonding (antisymmetric) mode, characterized by spatial field distributions $u_{1,2}(\mathbf{r})$ and frequencies $\omega_{1,2} = \omega_0 \mp \Delta\omega$, respectively. Here, $\Delta\omega$ is the mode detuning from the frequency of the single-cavity resonance, ω_0. For weak mode overlap, the spatial intensity profiles of two modes nearly coincide, $|u_1(r)|^2 \approx |u_2(r)|^2$. We assume that the cavities contain a laser medium with the gain centered at frequency $\omega_a = \omega_0 + \delta$, homogeneously broadened to have a line width of $\Delta\omega_a > \Delta\omega$, where δ is the detuning of the gain profile from the cavity frequency ω_0. See Fig. 7b for the definition of the frequency parameters. For the numerical calculations below, we take a quadratic array of 12×12 nanopillars with dielectric constant $\epsilon = 9$ in air ($\epsilon = 1$). The lattice period is $a = 500$ nm and the pillar radius $r = 0.2a$. Then both defect modes have frequencies near $a/\lambda \simeq 0.395$ (Fig. 7b).

To obtain an understanding of the seeding-induced mode switching, the semiclassical Maxwell–Bloch equations [50], may be simplified using the rotating-wave and the slowly varying envelope approximations. All the spatial dependencies of the electric field and atomic polarization can then be represented in the basis of the two cavity modes, such that $E(\mathbf{r}, t) = E_1(t)u_1(\mathbf{r})e^{-i\omega_1 t} + E_2(t)u_2(\mathbf{r})e^{-i\omega_2 t}$, etc., and the atomic polarization can be eliminated adiabatically [52, 53]. For class-A lasers, where the radiative decay rate $\gamma_\perp = \Delta\omega_a/2$, the nonradiative decay rate $\gamma_\parallel$, and the cavity mode

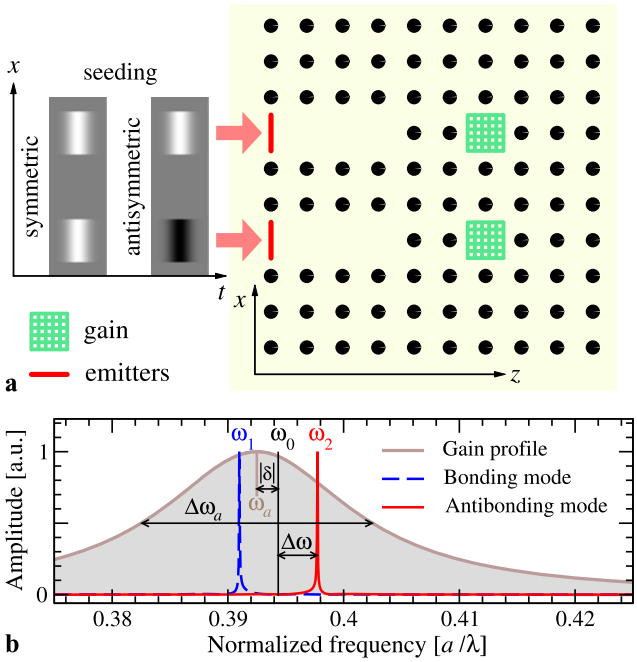

Fig. 7 (**a**) Schematic illustration of the resonant system under study. The two coupled defects in a periodic 2D PhC lattice contain a gain medium, shown in *green*. Two emitters shown are used to produce the seeding signal delivered to the defect sites by two waveguides. The spatial field distribution of the seeding signal is schematically depicted as a *gray scale* on the left, where *white* (*black*) refers to positive (negative) field strength. (**b**) Frequency parameters of the two-mode laser, see text

decay rates κ_j are related as $\gamma_\perp \gg \gamma_\parallel \gg \kappa_j$, the following system of equations for the slowly varying envelopes $E_j(t)$ in the two modes is obtained [52] ($i, j = 1, 2,\ i \neq j$),

$$\frac{dE_j(t)}{dt} = gR_j\left[\left(\mathcal{L}_j - \frac{\kappa_j}{gR_j}\right) - \eta\mathcal{L}_j\left(\alpha_{jj}^{jj}\mathcal{L}_j|E_j|^2 + \left[\alpha_{ii}^{jj}\mathcal{L}_i - \alpha_{ij}^{ji}\mathrm{Re}(\chi_j\mathcal{M}_{ji})\right]|E_i|^2\right)\right]E_j(t) + F_j(t). \tag{11}$$

In (11), the terms linear in $E_j(t)$ describe stimulated emission driving and are controlled by the light-matter coupling $g \simeq \sqrt{2\pi\omega_0 d^2/\hbar}$, with d the dipole moment of the atomic transition, by the pumping rates projected onto the modes $j = 1, 2$, $R_j = \int_G u_j^*(\mathbf{r})u_j(\mathbf{r})R(\mathbf{r})\,d\mathbf{r}$, and by the cavity mode decay rates κ_j. The coefficients $\mathcal{L}_j = \mathrm{Im}\,\beta_j^{-1}$, with $\beta_{1,2} = \delta \pm \Delta\omega - i\,\Delta\omega_a/2$, account for the different mode-to-gain couplings due to asymmetrical detuning of the atomic transition with respect to the resonator lines. The terms cubic in $E_j(t)$ describe field saturation above the lasing threshold, where $\eta = d^2/2\gamma_\parallel\hbar^2$ and the overlap integrals $\alpha_{kl}^{ij} = \int_G u_i^*(\mathbf{r})u_j(\mathbf{r})u_k^*(\mathbf{r})u_l(\mathbf{r})\,d\mathbf{r}$ are taken over the regions G containing the gain medium. Since $|u_1(r)|^2 \approx |u_2(r)|^2$ we can assume $\alpha_{jj}^{ii} = \alpha_{ji}^{ij} \equiv \alpha$, $R_1 = R_2 = R$ and $\kappa_1 = \kappa_2 = \kappa$.

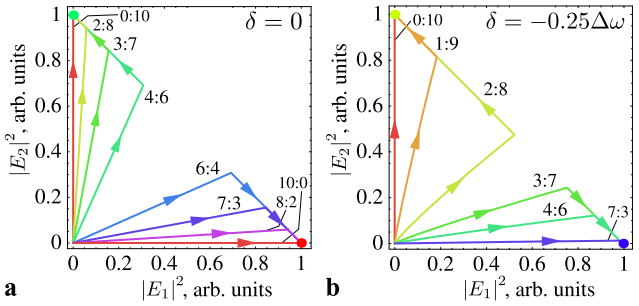

Fig. 8 Cavity phase diagrams for a lasing system governed by (11) for $F_j^s F(t) \gg F_j^n(t)$ for (**a**) symmetric ($\delta = 0$) and (**b**) nonsymmetric ($\delta = -0.25\Delta\omega$) values of the mode frequencies with respect to the central gain frequency ω_a ($\omega_a < \omega_0$, as shown in Fig. 7b). The dots denote the stable cavity states, and the curves represent the phase trajectories for their temporal evolution for different ratios $F_1^s : F_2^s$ in the direction of the *arrows*

The cross-saturation terms, with $\mathcal{M}_{ij} = \beta_i^{-1} + (\beta_j^*)^{-1}$ and $\chi_{1,2} = -i\gamma_\parallel/(\pm\Delta\omega - i\gamma_\parallel)$, depend in an asymmetrical way on the mode indices i, j. However, this asymmetry remains small unless $\Delta\omega \ll \Delta\omega_a$.

The inhomogeneous terms $F_j(t)$ originate from the external injection seeding field and from a noise field accounting for spontaneous emission [52]. For vanishing functions F_j, (11) would take the form of the standard two-mode competition equations [50] with mode coupling constant C slightly exceeding unity. This corresponds to bistable lasing [58, 59] and to mode hopping in the presence of stochastic noise in the system [60]. If both an external seeding field $\mathcal{E}^s(\mathbf{r}, t)$ and a stochastic noise field $\mathcal{E}^n(\mathbf{r}, t)$ are present in the cavity, $\mathcal{E}(\mathbf{r}, t) = \mathcal{E}^s(\mathbf{r}, t) + \mathcal{E}^n(\mathbf{r}, t)$, one obtains

$$F_j(t) \approx \frac{\omega_j \mathcal{L}_j}{\tau} \int_{t-\tau}^{t} dt' \, e^{i\omega_j t'} \int_G u_j(\mathbf{r}) \mathcal{E}(\mathbf{r}, t') \, d\mathbf{r} \tag{12}$$

$$= F_j^s F(t) + F_j^n(t). \tag{13}$$

The time integration in (13) is the averaging over a time interval larger than $1/\Delta\omega$. The function $F(t)$ is determined by the temporal dependence of $\mathcal{E}^s(\mathbf{r}, t)$. The coefficients F_j^s and $F_j^n(t)$ are determined by the spatial overlap of each mode with the seeding and noise fields, respectively. We consider the situation when the seeding prevails over the noise, i.e., $F_j^s F(t) \gg F_j^n(t)$, before and during the onset of lasing. After the onset the E_j become so large that the terms F_j have no effect anymore. In this situation, the evolution of the resonator will be determined by the ratio of F_1^s and F_2^s.

We analyze the influence of the balance between F_1^s and F_2^s on the final lasing state by numerical solution of (11) and plotting the phase trajectories of the temporal resonator state evolution in the ($|E_1|^2$, $|E_2|^2$) plane (Fig. 8). The numerical values of the coefficients in (11) are calculated for the model PhC structure of Fig. 7a. As seen in Fig. 8, the lasing state first reaches overall intensity saturation ($|E_1|^2 + |E_2|^2 = E_s^2$) and then drifts towards one of the stable fixed points corresponding to single-mode lasing (either $|E_1|^2 = E_s^2$ or $|E_2|^2 = E_s^2$). The drift occurs after the sharp bend seen in each of the phase trajectories. If the mode coupling constant is $C = 1$, the drift becomes infinitely slow, and the (1, 0)–(0, 1) line in Fig. 8 turns into a line of fixed points. For our case, where C only slightly exceeds unity, the drift happens on a longer time scale than the initial overall intensity growth, and the intermode beats decay fast after the lasing onset. In the case of symmetric detuning of the cavity modes with respect to the gain frequency ($\delta = 0$), single-mode lasing is achieved into that mode whose spatial overlap with the seeding field, F_j^s, is largest Fig. 8a. The asymmetry of the modes with respect to gain ($\delta \neq 0$) shifts the turning point toward one of the modes, but if the seeding is chosen in a way that the spatial overlaps in (13) result in $F_1^s \gg F_2^s$ or $F_1^s \ll F_2^s$, each of the modes can nonetheless be selected for lasing Fig. 8b.

To refine the predictions of this simple theory of bistable lasing, we have modeled the lasing action in coupled PhC defects with a realistic injection mechanism (Fig. 7) using the finite-difference time-domain (FDTD) method [61, 62]. The defect modes are located inside the PhC band gap. Both defects are filled with an active medium whose population dynamics are described at each space point by the rate equations of a four-level laser with an external pumping rate W_p. In defining the model and its parameter values we follow in detail [62, 63]. In particular, the nonradiative transition times of this model are taken so as to achieve population inversion, i.e., $\tau_{32} \simeq \tau_{10} \ll \tau_{21}$, with $\tau_{31} = \tau_{10} = 1 \times 10^{-13}$ s, $\tau_{21} = 3 \times 10^{-10}$ s, and the density of laser-active atoms (i.e., electrons participating in the lasing process) is $N_{\text{tot}} = 10^6/\mu\text{m}^3$ [63]. The Maxwell equations, supplemented by the usual equation of motion for the polarization density in the medium and by the laser rate equations [61–64], are solved for the geometry of Fig. 7a in TM polarization, where $\mathbf{E}(\mathbf{r}, t) = E_y(x, z, t)\,\hat{\mathbf{y}}$. The seeding signal is excited by two emitters (linear groups of dipoles) engineered on the same chip as the PhC and is transmitted to the defects through waveguides in the PhC (see Fig. 7). Each of the emitters generates a single short Gaussian pulse with carrier frequency ω at or near ω_a. The calculations have been performed using different, fixed values of the half-width duration σ_t in the range between $\sigma_t = 5 \times 10^{-14}$ and 10^{-13} s. The relative phase of the fields in these pulses is chosen 0 or π. As expected, such seeding patterns almost exclusively excite the bonding and antibonding mode, respectively. Technically, the seeding dipoles are realized as point-like oscillating current sources in the Maxwell equations [65]. Similarly, the spontaneous emission [62, 66, 67] is modeled as an ensemble of point current sources, randomly placed in space, with temporally δ-correlated Langevin noise [66]. For the

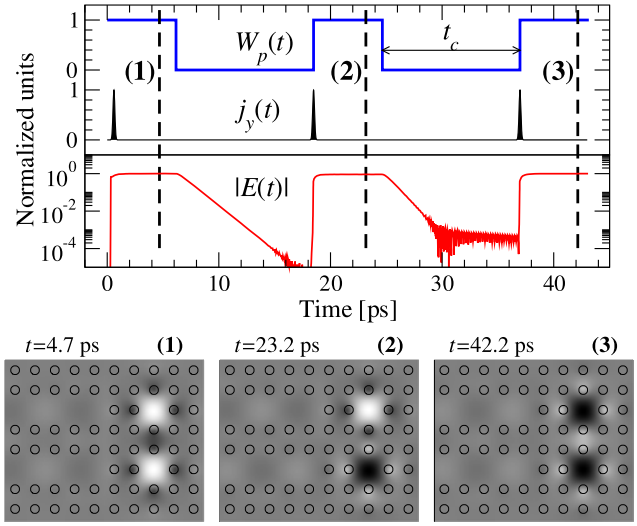

Fig. 9 Illustration of mode-to-mode switching. *Top*: time dependence of the normalized pumping power W_p, seeding signal j_y, and cavity field E_y. *Bottom*: spatial distribution of the electric field amplitude $E_y(x, z)$ (*gray scale*; *white*: positive; *black*: negative field strength) in the steady-state lasing regime after initial seeding (*1*) and each re-seeding (*2*, *3*). The time instants (*1–3*) are marked in the top panel by dashed lines. This calculation was done for a typical pumping rate $W_p = 1 \times 10^{13}$ s^{-1} and a seeding pulse duration $\sigma_t = 1.2 \times 10^{-13}$ s

FDTD computations, the computational domain $13a \times 13a$ with perfectly matched layer (PML) boundary conditions was discretized with an $a/16$ mesh and a time step of $dt = 6 \times 10^{-17}$ s required by numerical stability; see [68] for details.

Neglecting noise at first, we find that, if the laser amplification line spectrally covers both resonant modes and provides a comparable effective gain for each of them (i.e., $|\delta| < \Delta\omega$), a seeding signal of the type described above can individually select any of the two modes when applied (with arbitrary strength) during the onset of lasing, i.e., during the exponential growth after switching on the pumping. The steady-state lasing is then nearly single-mode, and the dominant mode is the one whose symmetry matches that of the seeding signal (Fig. 9). This is in agreement with the semi-analytical theory described above. The electric field maps in Fig. 9 (bottom) show that the spatial field distributions of the two lasing modes remain nearly unaffected by the side-coupled seeding waveguides. In the present setup, the laser output is primarily delivered through the seeding waveguides. A detailed study of the microlaser radiation characteristics will be given elsewhere. Moreover, we have shown that successive switchings from one mode to another are possible. To achieve this, the pump is first turned off to allow the currently lasing mode to decay. After a certain cool-down time τ_c, the pumping is turned back on, and the cavity is re-seeded for the other mode in the same way as the initial seeding occurred. Figure 9 demonstrates such a switching sequence from the bonding to the antibonding mode and back. The pump was kept on for a time needed to achieve quasicontinuous lasing, as confirmed by the temporal dependence of the cavity field. Looking at the spatial field distribution in this regime (panels (1–3) in Fig. 9), we make sure that the mode switching occurs in the desired order.

The switching time τ_s between two lasing modes is primarily controlled by the minimum cool-down time $\tau_{c,\min}$, i.e., by the relatively slow mode decay time, $\tau = 1/\kappa$, and hence by the cavity Q-factor $Q = \omega_j/\kappa$, not by the fast lasing onset after reseeding, $\tau_s \approx \tau_{c,\min}$. Since the mode decays exponentially with time from its steady-state lasing amplitude A_0 and the reseeding signal must be strong enough to override the residue of the decaying initial mode, $\tau_{c,\min}$ decreases logarithmically with increasing reseeding pulse power (i.e., with its time-integrated intensity) or, for a Gaussian pulse, with the seeding amplitude S, $\tau_{c,\min} = -(c_j/\kappa)\ln(S/A_0)$. Here, c_j is a dimensionless factor describing the coupling of the cavity mode $j = 1, 2$ to the laser transition. The corresponding numerical FDTD results are shown in Fig. 10. For realistic parameter values (Fig. 10), switching times of a few tens of picoseconds can be realized for reseeding amplitudes S as low as 0.001% of the lasing mode amplitude A_0, two to three orders of magnitude faster than in previous devices [69].

When noise is present in the cavity, the FDTD calculations show that controlled switching is preserved as long as the integrated seeding power exceeds the noise power integrated over the lasing onset time. Otherwise, noise begins to dominate the lasing spectrum formation. In this case, the mode whose spatial overlap with the noise field at the onset of lasing is larger wins the competition. The same happens when the seeding pulse does not match the onset of lasing in time and its field residue has smaller amplitude in comparison to the noise field. These numerical observations are fully consistent with the analysis of the competition equations (11) with the functions $F_j(t)$ given by (13). The switching is effective only if the influence of the seeding prevails in the resonator at the period of time when laser radiation starts to build up.

To summarize, the concept of *switchable* (rather than tunable) lasing in microstructures has been introduced. Instead of externally changing the parameters of a single-mode cavity, an inherently multimode cavity is used, and one of the modes is deliberately made to be dominant for lasing by means of injection seeding. This offers the possibility of all-optical frequency selection and switching in microlasers with particularly low switching times. As an example, we have investigated the mode switching in a system of two coupled defects in a 2D PhC lattice. For realistically chosen parameters, a mode-to-mode switching on the picosecond scale has been numerically demonstrated. The results are consistent with a qualitative semianalytical model. It shows

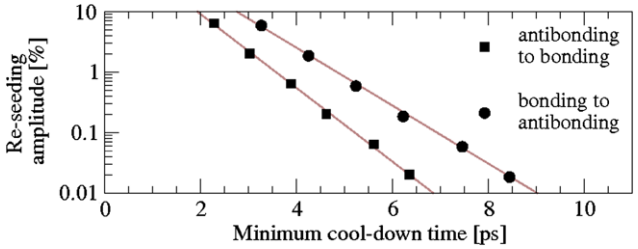

Fig. 10 The minimum switching time $\tau_{c,\min}$ versus the re-seeding amplitude, normalized to the saturated lasing mode amplitude. The seeding pulse duration is $\sigma_t = 0.12$ ps. The cavity mode decay time is $\tau = 0.7$ ps. The longer $\tau_{c,\min}$ for switching from the bonding to the antibonding mode is due to the nonzero gain detuning δ toward the bonding mode frequency (see Fig. 7b)

that a resonator supporting modes with similar spatial intensity profile tends towards bistability, which is the underlying physical mechanism of switchable lasing. The proposed concept is not limited to the model considered, but is expected to work in any resonator featuring bi- or multistability. Any coupled cavity based system would be a good candidate for the effects predicted.

4 Homogeneously disordered random lasers

A diffusive random laser is a system formed by randomly distributed scatterers embedded in a host medium where either scatterer or host medium or both provide optical gain through stimulated emission [14]. Recent observations of random lasing in a wide variety of systems [70–78] have triggered a rapidly growing interest. Random lasers share some properties with conventional lasers, like threshold behavior [72], narrow spectral lines [79], or photon statistics [80], but also exhibit distinctly different properties like multidirectional emission. Coherent feedback has unambiguously been demonstrated to be present in strongly disordered, homogeneous random lasers [80]. Its mechanism is multiple random scattering, possibly enhanced by self-interference of waves and the resulting onset of Anderson localization (AL) [15]. However, the scattering mean free path observed in these systems is by far too long for true Anderson localization to be realized. Therefore, the physical origin of coherent feedback, the origin of the spatially confined regions from which the laser emission takes place [73, 79], and the dependence of their size on the pump rate have remained controversial [79, 81, 82]. Our work provides a theory towards explaining these phenomena.

4.1 Definition of the model

The time evolution of the electric field distribution is parameterized as

$$\mathbf{E}(\mathbf{r},t) = \mathbf{E}^0(\mathbf{r},t)\, e^{-i\omega t}, \tag{14}$$

where ω is the laser frequency (i.e., the frequency of an electronic transition in an atom or dye molecule associated with the laser), and the electric field envelope $\mathbf{E}^0(\mathbf{r},t)$ varies slowly on the scale of $2\pi/\omega$. An analogous parameterization holds for the polarization $\mathbf{P}(\mathbf{r},t)$ of the laser medium. In class-B lasers, where the transverse relaxation rate is larger than the resonance detuning and the longitudinal relaxation rate [3], the polarization, $\mathbf{P}(\mathbf{r},t)$, follows the electric field $\mathbf{E}^0(\mathbf{r},t)$ instantaneously. Therefore, the lasing medium can effectively be described by a nonlinear dielectric constant $\epsilon(\mathbf{r},\mathbf{E}^0(\mathbf{r},t))$,

$$\mathbf{D}(\mathbf{r},t) = \mathbf{E}(\mathbf{r},t) + 4\pi\mathbf{P}(\mathbf{r},t) = \epsilon\big(\mathbf{r},\mathbf{E}^0(\mathbf{r},t)\big)\mathbf{E}(\mathbf{r},t). \tag{15}$$

Observing that the time dependence of $\mathbf{E}^0(\mathbf{r},t)$ is slow, the propagation of light is then described by the wave equation,

$$\frac{\omega^2}{c^2}\epsilon\big(\mathbf{r},\mathbf{E}^0(\mathbf{r},t)\big)\, E_\omega(\mathbf{r}) + \nabla^2 E_\omega(\mathbf{r}) = -i\omega\frac{4\pi}{c^2} j_\omega(\mathbf{r}), \tag{16}$$

where c denotes the vacuum speed of light and $j_\omega(\mathbf{r})$ an external current source. Note that for class-B lasers the full laser dynamics, including saturation, is incorporated in the highly nonlinear behavior of the dielectric constant $\epsilon(\mathbf{r},\mathbf{E}^0(\mathbf{r},t))$. The spatial dependence of the latter is further parameterized as $\epsilon(\mathbf{r}) = \epsilon_b + \Delta\epsilon V(\mathbf{r})$, where the dielectric contrast between the background, ϵ_b, and the scatterers, ϵ_s, has been defined as $\Delta\epsilon = \epsilon_s - \epsilon_b$. The spatial arrangement of the scatterers is described through the function $V(\mathbf{r}) = \sum_{\mathbf{R}} S_{\mathbf{R}}(\mathbf{r}-\mathbf{R})$, with $S_{\mathbf{R}}(\mathbf{r})$ a localized shape function at random locations $\mathbf{R}$. Linear gain (absorption) is described by a temporally constant, negative (positive) imaginary part of ϵ_b and/or ϵ_s.

4.2 Diffusion, linear gain and causality

In [83–85], we have developed a theory for light transport in disordered media with linear gain or absorption. It results in an energy–density correlation function $P_E^\omega(\mathbf{r}-\mathbf{r}', t-t')$, which describes how the energy density of the light field with frequency ω propagates diffusively between two points in space and time, $(\mathbf{r},t)$, $(\mathbf{r}',t')$. The Fourier transform of the energy–density correlation function $P_E^\omega(q,\Omega)$ is obtained as

$$P_E^\omega(q,\Omega) = \frac{N_P}{\Omega + iq^2 D + i\xi_a^{-2} D}, \tag{17}$$

where the expression for the coefficient N_P is given explicitly in [84], but is not relevant for the present purpose. It should be remarked that the correlator, (17), incorporates intensity correlations induced in the optical wave dynamics by the disorder, while quantum mechanical, spatiotemporal correlations, originating from the stimulated emission process in the atoms, will be neglected by using the semiclassical laser rate equations below. The denominator of (17)

exhibits the expected diffusion pole structure with the diffusion coefficient D. In addition, in the case of a nonconserving medium, i.e., net absorption (gain), there appears the (purely imaginary) term $i\gamma_a = i\xi_a^{-2}D$, which has a positive (negative) imaginary part and does not vanish in the hydrodynamic limit, $\Omega \to 0,\ q \to 0$. The self-consistent solution of the transport theory including self-interference of waves (Cooperon contributions) (see [84]) shows that in the presence of absorption or gain the diffusion coefficient D cannot vanish and is in general complex. Hence, truly Anderson localized modes do not exist in this case.

For the case of absorption ($\gamma_a > 0$), it is seen by Fourier transforming (17) w.r.t. time, $P_E^{\omega}(q,t) = iN_P\, e^{-(q^2D+\gamma_a)t}$, that $\mathrm{Re}\,\gamma_a$ represents the loss rate of the photonic energy density due to absorption in the medium. Fourier transforming, on the other hand, (17) w.r.t. space in the stationary limit ($\Omega \to 0$)) shows that $\xi_a = \mathrm{Re}\sqrt{(\gamma_a/D)}$ is the length scale over which the energy density of diffusive modes is correlated in the lossy medium.

For the case of linear gain ($\gamma_a < 0$), the wave equation predicts an unlimited growth of the field amplitude, and hence of the energy density. This means that a stationary lasing state is not possible in this case and, therefore, the limit $\Omega \to 0$ must strictly not be taken in (17). Such a behavior of linear gain is expected only during the exponential intensity growth shortly after the onset of lasing. A complete theory of random lasing must, therefore, take into account either the full temporal dynamics of the system, or in a stationary state additional surface loss effects must compensate for the gain in the medium (see Sect. 4.3). Nevertheless, we can extract a characteristic size of a stationary lasing spot from this theory by requiring that the stationary lasing state has been reached *locally*, i.e., within a finite subvolume of the system: Causality requires that the pole of $P_E^{\omega}(q,\Omega)$, (17), as a function of Ω resides in the lower complex Ω halfplane. For $\gamma_a < 0$, this is possible only if all the diffusive modes allowed inside a given lasing spot have a wavenumber $q > q_{\min} = \sqrt{\mathrm{Re}(-\gamma_a/D)}$. This, in turn, requires that the spot size is [17, 18]

$$R_s = \frac{2\pi}{q_{\min}} = \frac{2\pi}{\sqrt{\mathrm{Re}(-\gamma_a/D)}}. \tag{18}$$

It is the characteristic, maximal size of a spatial region over which diffusive modes can be causally correlated in the stationary lasing state. We conjecture that, hence, this size is to be identified with the lasing spot size observed experimentally [73, 79] in random lasers.

More generally, despite the fact that the linear gain assumption is not suited to describe stationary lasing, it can be used to estimate the laser threshold, i.e., the critical pump rate for lasing. Amazingly, this is a rather general remark. For example, in a simpler system of a single microsphere

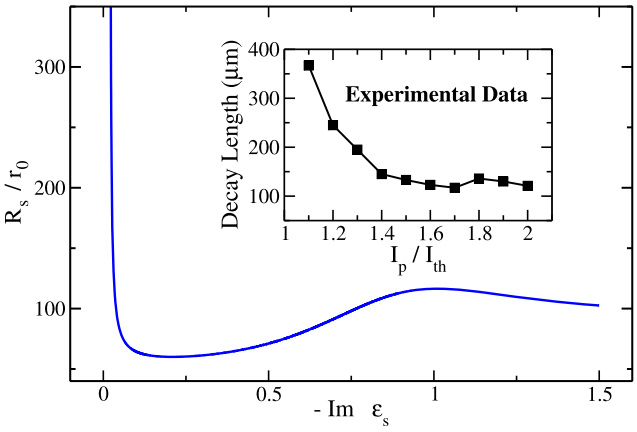

Fig. 11 The spot size R_s (18) in units of the scatterer radius r_0, as obtained by causality considerations as a function of the imaginary part of the dielectric constant of the scatterers [17]. The parameter values used are $\epsilon_b = 1$, $\mathrm{Re}\,\epsilon_s = 10$, scatterer filling fraction $\nu = 30\%$, light frequency $\omega/\omega_0 = 2.5$. The light frequency is $\omega_0 = 2\pi c/r_0$ where c is the vacuum speed of light. The data in the inset are taken from [73] and refer to the spot size of the modes

with gain, it has been shown [16], that the scattering coefficients calculated within linear response lose their causality just at the point where the sphere crosses its lasing threshold. Applied to our random laser system, this means that the threshold for lasing within a spot of size R_s is reached when the transport coefficient $-\gamma_a$, determined by the pump rate via the microscopic transport theory [83, 84], reaches the value given by (18).

In Fig. 11, we show the numerical evaluation of the spot size R_s as a function of increasing $\mathrm{Im}\,\epsilon_s$ for typical parameters, as given in the figure caption. The imaginary part of the dielectric constant is a measure of external pumping, since the gain is given by the population inversion of the laser. Therefore, larger pumping yields higher inversion and leads to a larger $\mathrm{Im}\,\epsilon_s$. The calculated spot size reproduces the essential features of the behavior of the experimental data [73] (spot size vs. pump intensity normalized to the threshold intensity), shown in the inset.

4.3 Selfconsistent, nonlinear theory of random lasing

As remarked above, a stationary lasing state in a homogeneously pumped system is possible only if the system is finite, so that surface loss effects can compensate the gain in the medium. To avoid the causality problem, we consider here a three-dimensional random laser model with a homogeneously pumped, active medium which extends infinitely in the (x, y) plane, but has a finite, constant thickness d in the z direction. The laser-active material is described by the semiclassical laser rate equations, and the light intensity transport by a diffusion equation. In particular, the rate equations for a four-level laser

are

$$\frac{\partial N_3}{\partial t} = \frac{N_0}{\tau_P} - \frac{N_3}{\tau_{32}}, \tag{19}$$

$$\frac{\partial N_2}{\partial t} = \frac{N_3}{\tau_{32}} - \left(\frac{1}{\tau_{21}} + \frac{1}{\tau_{\mathrm{nr}}}\right) N_2 - \frac{(N_2 - N_1)}{\tau_{21}} n_{\mathrm{ph}}, \tag{20}$$

$$\frac{\partial N_1}{\partial t} = \left(\frac{1}{\tau_{21}} + \frac{1}{\tau_{\mathrm{nr}}}\right) N_2 + \frac{(N_2 - N_1)}{\tau_{21}} n_{\mathrm{ph}} - \frac{N_1}{\tau_{10}}, \tag{21}$$

$$\frac{\partial N_0}{\partial t} = \frac{N_1}{\tau_{10}} - \frac{N_0}{\tau_P}, \tag{22}$$

$$N_{\mathrm{tot}} = N_0 + N_1 + N_2 + N_3, \tag{23}$$

where $N_i = N_i(\mathbf{r}, t)$, $i = 0,\ 1,\ 2,\ 3$ are the population number densities of the corresponding electron level ($i \in \{1 \ldots 4\}$), N_{tot} is the total number of electrons participating in the lasing process, $\gamma_{ij} \equiv 1/\tau_{ij}$ are the transition rates from level i to j, and γ_{nr} is the nonradiative decay rate of the laser level 2. $\gamma_P \equiv 1/\tau_P$ is the transition rate due to homogeneous, constant, external pumping. Furthermore, $n_{\mathrm{ph}} \equiv N_{\mathrm{ph}}/N_{\mathrm{tot}}$ is the photon number density, normalized to N_{tot}. In the stationary limit (i.e., $\partial_t N_i = 0$), the above system of equations can be solved for the population inversion $n_2 = N_2/N_{\mathrm{tot}}$ to yield (γ_{32} and γ_{10} assumed to be large compared to all other rates)

$$n_2 = \frac{\gamma_P}{\gamma_P + \gamma_{\mathrm{nr}} + \gamma_{21}(n_{\mathrm{ph}} + 1)}. \tag{24}$$

The photon number density (light intensity), normalized to N_{tot}, $n_{\mathrm{ph}} = N_{\mathrm{ph}}/N_{\mathrm{tot}}$, obeys the diffusion equation [19],

$$\partial_t n_{\mathrm{ph}} = D_0 \nabla^2 n_{\mathrm{ph}} + \gamma_{21}(n_{\mathrm{ph}} + 1) n_2, \tag{25}$$

where the last term on the r.h.s. describes the intensity increase due to stimulated and spontaneous emission, as described by the semi-classical laser rate equations. Since in the slab geometry ensemble-averaged quantities are translationally invariant in the (x, y) plane, but not along the z direction, a Fourier representation in the (x, y) plane in terms of $n_{\mathrm{ph}}(\mathbf{q}_\parallel, z)$, $n_2(\mathbf{q}_\parallel, z)$ is convenient,

$$\partial_t n_{\mathrm{ph}} = -D_0 q_\parallel^2 n_{\mathrm{ph}} + D_0 \partial_z^2 n_{\mathrm{ph}} + \gamma_{21} \int \frac{d^2 q'_\parallel}{(2\pi)^2} n_{\mathrm{ph}}\left(\mathbf{q}_\parallel - \mathbf{q}'_\parallel, z\right) n_2\left(\mathbf{q}'_\parallel, z\right) + \gamma_{21} n_2. \tag{26}$$

We now determine the photon density response function $P(\mathbf{q}_\parallel, z, \Omega)$, which describes the response of the photon density, n_{ph}, to the distribution of the population inversion, n_2, in order to determine the transport coefficients. In the stationary case ($\partial_t n_{\mathrm{ph}} = 0$) and in the long-wavelength limit along the (x, y) plane ($q_\parallel \to 0$), the z derivative in (26) can be expressed without derivatives in terms of n_{ph} and n_2 only. Plugging this back into (26) yields,

$$\left[\partial_t + D_0 q_\parallel^2 + \frac{\gamma_{21} n_2}{n_{\mathrm{ph}}}\right] n_{\mathrm{ph}}(\mathbf{q}_{\parallel,z}, t) = \gamma_{21} n_2(\mathbf{q}_{\parallel,z}, t) \tag{27}$$

and hence after Fourier transform w.r.t. time, the diffusion form of the density response function,

$$P_E(\mathbf{q}_\parallel, z, \Omega) = \frac{i\gamma_{21}}{\Omega + i q_\parallel^2 D_0 + i\xi^{-2} D_0}, \tag{28}$$

where from (27) the correlation length ξ is defined as the real, positive quantity,

$$\xi = \sqrt{\frac{D_0}{\gamma_{21}} \frac{n_{\mathrm{ph}}}{n_2}}. \tag{29}$$

As seen from (28), the pole structure in this finite-size, diffusive system is perfectly causal. The square of the correlation length ξ remains positive, indicating an effective loss out of a given $q_\parallel$ mode. This is due to the loss of intensity at the surfaces. Additionally, the mass term becomes less and less significant as the laser intensity in the sample builds up, because the relative population inversion clearly obeys $n_2 \leq 1$ whereas the relative photon number is not restricted.

Since for homogeneous pumping the averaged photon density does not depend on x or y, (26) simplifies in the stationary limit to

$$D_0 \partial_z^2 n_{\mathrm{ph}} = -\gamma_{21}(n_{\mathrm{ph}} + 1) n_2 \tag{30}$$

and $n_{\mathrm{ph}}(z)$ is finally determined via (24) by the regular differential equation,

$$\partial_z^2 n_{\mathrm{ph}}(z) = -\frac{\gamma_{21}}{D_0} \frac{(\gamma_P/\gamma_{21})}{1 + \frac{(\gamma_P/\gamma_{21})}{n_{\mathrm{ph}}(z)+1}}. \tag{31}$$

Equations (31), (24), and (29) comprise the complete description of the spatial photon density profile perpendicular to the lasing film and the intensity correlation length (spot size) parallel to the film.

Numerical evaluations of (31), (29), and (24) are shown in Figs. 12 and 13. In Fig. 12, the photon number $n_{\mathrm{ph}}(z)$, population inversion $n_2(z)$ and correlation length $\xi(z)$ are shown as a function of z for different values of external pumping, characterized by the pumping rate γ_P. The value of the diffusion constant was chosen to be $D_0 = 1 d^2 \gamma_{21}$, where d is the width of the film. In panel a) of Fig. 12, the photon number displays a monotonically increasing behavior with increasing pumping. The maximum of the intensity resides in the center of film ($z = 0$), since this is the position farthest from the boundaries and, therefore, with lowest

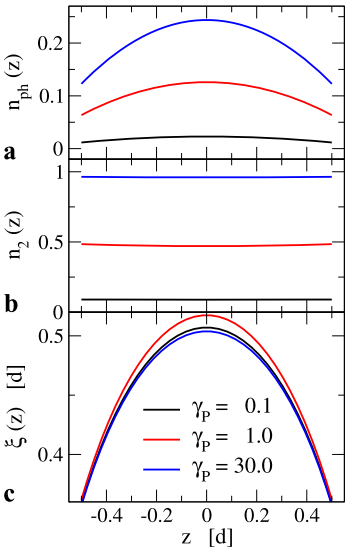

Fig. 12 The following quantities are shown as a function of z for different values of the pump rate P: (**a**) the photon number, which increases monotonically with increasing pump rate and has its maximum in the film center ($z = 0$); (**b**) the population inversion, which is inverse proportional to $n_{\rm ph}$, see (24); (**c**) the correlation length (spot size), which clearly behaves nonmonotonically with increasing pumping. The diffusion constant in all panels is $D_0 = 1d^2\gamma_{21}$

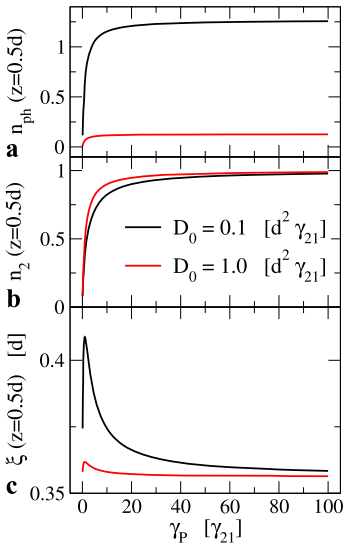

Fig. 13 The figure shows the following quantities as a function of the pumping rate P at the film surface ($z = \pm 0.5d$): (**a**) the photon number which displaying saturation for strong pumping; (**b**) the population inversion, also saturating; (**c**) the correlation length (spot size) showing nonmonotonic behavior (discussion in the text)

loss of intensity. The population inversion, (24), behaves inverse to $n_{\rm ph}(z)$; see (24). In contrast to this rather expected behavior, the correlation length $\xi(z)$ as given by (29) exhibits a nonmonotonic behavior with increasing pumping. For pumping rates $\gamma_P < \gamma_{21}$, the correlation length increases but for pumping rates $\gamma_P > \gamma_{21}$, ξ is decreasing. The equality between γ_P and γ_{21} marks the situation where electrons are as fast excited into the upper laser level as they relaxate to lower levels. Therefore, this characterizes the lasing threshold. Available experimental data [73, 79] also report a decreasing behavior of the spot size above threshold. Measurements of the intensity correlation length below threshold have not been reported yet.

The same quantities are shown Fig. 13 as a function of external pumping at the surface of the random laser. Photon number and population inversion both display saturation behavior. Panel c of Fig. 13, however, exhibits the nonmonotonic behavior of the correlation length. This plot is to be directly compared to experimental data [73] as, e.g., shown in the inset of Fig. 12. There is a good qualitative and even quantitative agreement between calculated and measured spot size.

5 Extension of semiclassical microlaser theory to arbitrary nonlinearity

In the standard semiclassical laser theory [2, 3], lasing modes are usually taken to coincide with quasimodes of the respective cavities, while their amplitudes and frequencies are found from equations based on perturbation expansions containing terms linear and cubic in the field. In random lasers, this picture needs to be revised. It was shown [20, 21] that normal modes in the presence of gain differ from the passive modes even in the linear approximation, if the refractive index and/or unsaturated population inversion are nonuniform. Furthermore, it was realized [86–88] that the self- and cross-saturation coefficients before the cubic terms can have different statistical properties in different systems, leading to different mode statistics. Finally, it was pointed out [22, 23] that nonlinear effects can significantly contribute to modification of the lasing modes compared to those of the empty cavity.

In [24], we carried out the perturbation expansion up to the infinite order in the field keeping all the terms which do not have fast temporal oscillations. To that end, a novel diagram technique was developed which allows for a systematic classification of all terms of the expansion. In contrast to the approach of [22, 23], no assumption of constant population inversion was introduced. In the following, starting from the semiclassical laser equations, we review the diagrammatic technique and the first application of the infinite-order expansion to the case of chaotic gas lasers where, due to the thermal motion of the atoms, the Doppler shift of the emission frequencies is not small.

5.1 Semiclassical laser equations

In the semiclassical theory of lasers [2, 3], the fields are described classically at the level of Maxwell equations and the

active medium is treated by quantum mechanics. To this end, the wave equation for the electric field $E(\mathbf{r},t)$ is written with a source term, the polarization $P(\mathbf{r},t)$ of the gain medium:

$$\epsilon(\mathbf{r})\frac{\partial^2}{\partial t^2}E-\nabla^2 E=-4\pi\frac{\partial^2}{\partial t^2}P(\mathbf{r},t). \tag{32}$$

Here $\epsilon(\mathbf{r})$ is the (real) dielectric constant and we use the units where the velocity of light $c=1$. In the simplest model, the active medium is a collection of homogeneously broadened two-level atoms. Their state is fully described by $P(\mathbf{r},t)$ and the population-inversion density $\Delta n(\mathbf{r},t)$ (difference between populations of the upper and lower levels per unit volume). These functions satisfy the equations of motion [3]

$$\left(\frac{\partial^2}{\partial t^2}+2\gamma_\perp\frac{\partial}{\partial t}+\nu^2\right)P=-2\nu\frac{d^2}{\hbar}E(\mathbf{r},t)\,\Delta n(\mathbf{r},t), \tag{33}$$

$$\frac{\partial}{\partial t}\Delta n-\gamma_\parallel\big[\Delta n_0(\mathbf{r},t)-\Delta n\big]=\frac{2}{\hbar\nu}E(\mathbf{r},t)\frac{\partial}{\partial t}P(\mathbf{r},t), \tag{34}$$

where d is the magnitude of the atomic dipole matrix element, ν is the atomic transition frequency, and $\gamma_\perp$ ($\gamma_\parallel$) is the polarization (population-inversion) decay rate. If the right-hand side of (34) vanishes, Δn relaxes to the unsaturated population inversion $\Delta n_0(\mathbf{r},t)$, which is a measure of the pump strength. The coupled equations (32)–(34) determine, in principle, the electric field in the system, if $\Delta n_0(\mathbf{r},t)$ is given.

In a system with N_m lasing modes the electric field can be approximately represented as a sum of oscillating terms

$$E(\mathbf{r},t)=\mathrm{Re}\sum_{l=1}^{N_\mathrm{m}}E_l(\mathbf{r},t)e^{-i\omega_l t}, \tag{35}$$

where ω_l is the frequency of mode l and $E_l(\mathbf{r},t)$ is its slowly varying amplitude. It is convenient to expand the electric field in an open cavity in a biorthogonal basis as

$$E_l(\mathbf{r},t)=\epsilon^{-1/2}(\mathbf{r})\sum_k a_{lk}(t)\,\psi_k(\mathbf{r},\omega_l), \tag{36}$$

$$a_{lk}(t)=\int d\mathbf{r}\,\epsilon^{1/2}(\mathbf{r})\,\phi_k^*(\mathbf{r},\omega_l)\,E_l(\mathbf{r},t), \tag{37}$$

where $\psi_k(\mathbf{r},\omega)$ and $\phi_k(\mathbf{r},\omega)$ are the biorthogonal basis modes parameterized by the frequency [22].

Equations (32)–(34) can be reduced to an equation for the electric field alone using perturbation theory in the field amplitude. In particular, one needs to construct an expansion of $P(\mathbf{r},t)$ in the (odd) powers of the field using (33) and (34). Then this expansion is substituted in (32) producing the required equation for the field. In the conventional laser theory [2, 3], $P(\mathbf{r},t)$ is expanded up to the third order in $E(\mathbf{r},t)$, which yields the saturation terms in the rate equations. Here, we carry out the expansion up to an arbitrary order in the field's amplitude and use a diagrammatic method to sort out the respective terms.

The perturbative expansion of (32)–(34) yields equations for the coefficients $a_{lk}(t)$:

$$\left[-i\frac{d}{d}t+\Omega_k(\omega_l)-\omega_l\right]a_{lk}(t)$$
$$=2\pi\nu\sum_{k'}a_{lk'}(t)\int d\mathbf{r}\,\epsilon^{-1}(\mathbf{r})\phi_k^*(\mathbf{r},\omega_l)\,\psi_{k'}(\mathbf{r},\omega_l)\eta_l(\mathbf{r},t), \tag{38}$$

where $\Omega_k(\omega)$ are complex eigenfrequencies (similar to resonances) corresponding to the basis modes $\psi_k(\mathbf{r},\omega)$ and $\phi_k(\mathbf{r},\omega)$. The right-hand side has a nonlinear dependence on the electric field via the susceptibility in the mode l,

$$\begin{aligned}
&\eta_l(\mathbf{r},t)\\
&\equiv\frac{P_l(\mathbf{r},t)}{E_l(\mathbf{r},t)}=2i\hbar\gamma_\parallel D(\omega_l)\Delta n_0(\mathbf{r})\sum_{q\ \mathrm{odd}}A^{\frac{q+1}{2}}\\
&\quad\times\sum_{l_1,\ldots,l_q}^{\mathrm{r}}\left|E_{l_2}(\mathbf{r},t)\right|^2\left|E_{l_4}(\mathbf{r},t)\right|^2\cdots\left|E_{l_{q-1}}(\mathbf{r},t)\right|^2\\
&\quad\times D_\parallel(\omega_{l_1}-\omega_{l_2})\,D_\parallel(\omega_{l_1}-\omega_{l_2}+\omega_{l_3}-\omega_{l_4})\cdots\\
&\quad\times D_\parallel(\omega_{l_1}-\omega_{l_2}+\cdots+\omega_{l_{q-2}}-\omega_{l_{q-1}})\\
&\quad\times\left[D(\omega_{l_1})+D^*(\omega_{l_2})\right]\\
&\quad\times\left[D(\omega_{l_1}-\omega_{l_2}+\omega_{l_3})+D^*(\omega_{l_2}-\omega_{l_1}+\omega_{l_4})\right]\cdots\\
&\quad\times[D(\omega_{l_1}-\omega_{l_2}+\omega_{l_3}-\cdots-\omega_{l_{q-3}}+\omega_{l_{q-2}})\\
&\quad+D^*(\omega_{l_2}-\omega_{l_1}+\omega_{l_4}-\cdots-\omega_{l_{q-4}}+\omega_{l_{q-1}})],
\end{aligned} \tag{39}$$

where

$$A\equiv-\frac{d^2}{2\hbar^2\gamma_\perp\gamma_\parallel}, \tag{40}$$

$$D(\omega)\equiv\left[1-i\frac{\omega-\nu}{\gamma_\perp}\right]^{-1}, \tag{41}$$

$$D_\parallel(\omega)\equiv\left[1-i\frac{\omega}{\gamma_\parallel}\right]^{-1}. \tag{42}$$

The order of nonlinearity q determines the number of different indices l_i, which take values from 1 to N_m. The superscript "r" at the sum symbol specifies that the possible values of the indices are restricted by the resonance condition

$$\omega_{l_1}-\omega_{l_2}+\omega_{l_3}-\cdots-\omega_{l_{q-1}}+\omega_{l_q}-\omega_l=0, \tag{43}$$

which ensures *cancellation of fast oscillating terms*. In the absence of accidental degeneracies, this condition implies that each of the indices $l_1,l_3,\ldots,l_q$ must be equal to one of

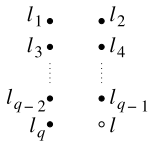

Fig. 14 Labeling of vertices in a diagram of order $q = 1, 3, \ldots$

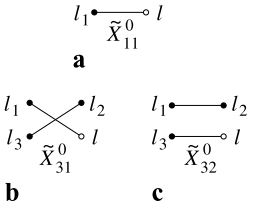

Fig. 15 First-order diagram (**a**) and third-order diagrams (**b**, **c**)

the indices $l_2, l_4, \ldots, l_{q-1}, l$. This leads, in particular, to the appearance of absolute squares of the field in the first line of (39).

The nonlinear equations (38) have to be solved in a self-consistent way to determine the number of modes N_m, their frequencies ω_l, and the coefficients $a_{lk}(t)$.

5.2 Diagrammatic technique

We use diagrams to classify different pairing possibilities for the lasing mode indices $l_1, l_2, \ldots, l_q, l$ in the perturbation series (39). To construct a diagram $\widetilde{X}^0_{qj}$ of order $q = 1, 3, \ldots$, we place $q + 1$ vertices in two columns as shown in Fig. 14. The left vertices are labeled $l_1, l_3, \ldots, l_q$ and the right vertices are labeled $l_2, l_4, \ldots, l_{q-1}, l$. The vertex l is different from the other vertices, because there is no summation over the index l in (39). After that, each vertex on the left is connected with exactly one vertex on the right. The index $j = 1, \ldots, \widetilde{N}_q$ labels all distinct connection possibilities in an arbitrary order. To obtain all diagrams of order q, we can first connect the vertices by $(q + 1)/2$ horizontal links and then reshuffle the vertices, say, on the left without cutting the links. Thus, the number of possible diagrams of order q is the number of permutations $\widetilde{N}_q = [(q + 1)/2]!$. The diagrams for $q = 1, 3$ are shown in Fig. 15.

Each diagram specifies a particular contribution to the series (39). The latter will be written in the form

$$\eta_l(\mathbf{r}, t) = 2i\hbar\gamma_\parallel \Delta n_0(\mathbf{r})\, D(\omega_l)\mathcal{X}_l, \tag{44}$$

$$\mathcal{X}_l \equiv \sum_{q\ \text{odd}} A^{\frac{q+1}{2}} \sum_{j=1}^{\widetilde{N}_q} \widetilde{X}^0_{qj}, \tag{45}$$

where each $\widetilde{X}^0_{qj}$ represents a partial sum in $\sum^r(\cdots)$, (39), in which pairs of indices are chosen to be equal to each other according to the links connecting respective vertices in the diagram. For example, the first three diagrams correspond to the following expressions:

$$\widetilde{X}^0_{11} = 1, \tag{46}$$

$$\widetilde{X}^0_{31} = \sum_{l_2 \neq l} \big|E_{l_2}(\mathbf{r}, t)\big|^2 D_\parallel(\omega_l - \omega_{l_2})\big[D(\omega_l) + D^*(\omega_{l_2})\big], \tag{47}$$

$$\widetilde{X}^0_{32} = \sum_{l_2} \big|E_{l_2}(\mathbf{r}, t)\big|^2 2\,\mathrm{Re}\big[D(\omega_{l_2})\big]. \tag{48}$$

The restriction $l_2 \neq l$ in the diagram $\widetilde{X}^0_{31}$ excludes the term with $l_1 = l_2 = l_3 = l$, which enters $\widetilde{X}^0_{32}$. In general, the terms with more than two indices equal belong to the diagram in which the links connecting these indices do not cross each other.

A diagram is called connected, if it cannot be cut by a horizontal line without cutting a link. For instance, the diagrams $\widetilde{X}^0_{11}$ and $\widetilde{X}^0_{31}$ are connected, whereas the diagram $\widetilde{X}^0_{32}$ is disconnected. To simplify the notation, we ordered all connected diagrams before the disconnected diagrams for given q. We will label connected diagrams as X^0_{qj}, with

$$X^0_{qj} = \widetilde{X}^0_{qj}, \quad j = 1, \ldots, N_q, \tag{49}$$

where N_q $(< \widetilde{N}_q)$ is the number of connected diagrams. The horizontal cuts separate disconnected diagrams into one connected diagram containing the vertex l (denoted by an unfilled dot in the graphic representation) and several connected subdiagrams without such vertex. The latter subdiagrams will be denoted as X_{qj}, $j = 1, \ldots, N_q$, where $q + 1$ is the number of vertices in the subdiagram. In place of the vertex l, these diagrams have a vertex with the index l_{q+1} which runs over all lasing modes, as the other indices l_j. For example,

$$X_{11} = \sum_{l_2} \big|E_{l_2}(\mathbf{r}, t)\big|^2 2\,\mathrm{Re}\big[D(\omega_{l_2})\big], \tag{50}$$

$$X_{31} = \sum_{\substack{l_2, l_4 \\ l_2 \neq l_4}} \big|E_{l_2}(\mathbf{r}, t)\big|^2 \big|E_{l_4}(\mathbf{r}, t)\big|^2 \times D_\parallel(\omega_{l_4} - \omega_{l_2})\big[D(\omega_{l_4}) + D^*(\omega_{l_2})\big]^2. \tag{51}$$

Note that X_{qj} is of the order $q + 1$ in the electric field. Connected diagrams contain $(q - 1)/2$ factors $D_\parallel \neq 1$.

The diagrammatic technique possesses the basic property that disconnected diagrams are given by products of their connected parts, e.g., $\widetilde{X}^0_{32} = X^0_{11} X_{11}$. The multiplicativity is due to the fact that the resonance condition of the type (43) is fulfilled for each connected subdiagram. The multiplicativity property allows one to express the series (45) in terms of the *connected* diagrams as

$$\mathcal{X}_l = \left(\sum_{q\ \text{odd}} \sum_{j=1}^{N_q} X^0_{qj}\right) \sum_{m=0}^{\infty} \left(\sum_{q\ \text{odd}} \sum_{j=1}^{N_q} X_{qj}\right)^m$$

$$= \frac{\sum_{q \text{ odd}} \sum_{j=1}^{N_q} X_{qj}^0}{1 - \sum_{q \text{ odd}} \sum_{j=1}^{N_q} X_{qj}}. \quad (52)$$

The contributions X_{qj}^0 and X_{qj} contain the terms of the power $q-1$ and $q+1$ in the field, respectively. They are of the order $(q-1)/2$ in the small parameter $\gamma_\parallel/\gamma_\perp$ due to the factors $D_\parallel(\omega_l - \omega_{l'}) \sim \gamma_\parallel/(\omega_l - \omega_{l'}) \sim \gamma_\parallel/\gamma_\perp$. This parameter is a measure of the importance of taking into account the population oscillations in the laser equations. Thus, (52) is a perturbation expansion in $\gamma_\parallel/\gamma_\perp$, but it takes into account the amplitudes of the electric field up to *infinite* order.

The known special cases can be reproduced with the help of (52). To obtain an approximation to $\mathcal{X}_l$ of the third-order in the field, we keep the diagrams X_{11}^0 and X_{31}^0 in the numerator and the diagram X_{11} in the denominator of (52) and expand the latter:

$$\mathcal{X}_l \approx X_{11}^0 + X_{11}^0 X_{11} + X_{31}^0. \quad (53)$$

In the approximation of constant population inversion only the diagrams X_{11}^0 and X_{11}, which do not contain the $D_\parallel$ functions, contribute to $\mathcal{X}_l$. With the help of (52) it is straightforward to write out the corrections due to the population pulsations. The terms of the first order in $D_\parallel \ll 1$ are contained in the diagrams X_{31}^0 and X_{31}, so that $\mathcal{X}_l$ can be approximated as

$$\mathcal{X}_l \approx \frac{X_{11}^0 + X_{31}^0}{1 - X_{11} - X_{31}}. \quad (54)$$

5.3 Semiclassical theory of a gas laser

The generalized semiclassical laser theory (up to the third order in the field) was applied to gas lasers with *wave-chaotic resonators* in [25]. Gas lasers can emit light at frequencies that differ from the atomic transition frequency by more than a homogeneous linewidth $\gamma_\perp$ [2, 3]. This property is a consequence of the coherent amplification by moving atoms that interact with the electric field at Doppler-shifted frequencies. The inhomogeneous linewidth is approximately $q_0\overline{v} \gg \gamma_\perp$, where $q_0 = \sqrt{\epsilon}\nu/c$ is the wavenumber at the atomic transition frequency and $\overline{v}$ is the average velocity of atoms.

The notion of a chaotic system implies that the shape of the resonator does not permit a separation of variables in the wave equation and the relevant modes have a typical wavelength λ much smaller than the system size. The classical ray dynamics, defined in the short-wavelength limit, is assumed to be ergodic, i.e., the generic ray trajectories fill densely the available phase space. The eigenmodes of a chaotic resonator are spatially uncorrelated outside of the correlation volume $\sim\lambda^3$, i.e., $\langle\psi_k(\mathbf{r})\psi_k(\mathbf{r}')\rangle = 0$ if $|\mathbf{r} - \mathbf{r}'| \gg \lambda$. The eigenfunctions of the resonator can be locally approximated by a superposition of plane waves with a fixed wavelength propagating in random directions.

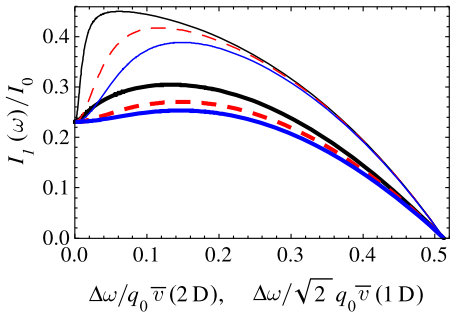

Fig. 16 Relative intensity of the single lasing mode for the two-dimensional (2D) chaotic laser (*thick curves*) and a one-dimensional (1D) laser (*thin curves*) as a function of the frequency separation $\Delta\omega$ from the atomic-line center. The scaling of $\Delta\omega$ for these systems differs by a factor of $\sqrt{2}$. Relative homogeneous linewidth $\gamma_\perp/q_0\overline{v} = 0.01$ (*solid curves*), 0.04 (*dashed curves*), and 0.07 (*dash-dotted curves*). The pump strength parameter Δn_0 is 30% above the threshold value. I_0 is defined as $I_1(\nu)$ extrapolated to $\Delta n_0 \to \infty$

If a resonance frequency of the cavity is continuously changed, the intensity of the single mode has a minimum at the atomic frequency (Fig. 16). In uniaxial (quasi-one-dimensional) cavities this minimum, called the Lamb dip [89], has a width of $\sim\gamma_\perp$. In two-dimensional weakly open cavities of chaotic geometry, the width of the minimum is comparable to the *inhomogeneous* linewidth $q_0\overline{v}$. In Fig. 16, the scaling of the minimum width with $\gamma_\perp$ can be clearly seen for a one-dimensional laser, whereas the scaling is absent in two dimensions [25].

6 Conclusion

To summarize, spatially confined modes and field distributions with finite correlation length play important roles in photonic systems, let them be cavity or defect modes in photonic crystals, lasing spots in diffusive random lasers, or the lasing modes in chaotic microlaser cavities. To describe such systems with localized field distributions, a large variety of theoretical methods is needed, due to their different physical nature.

For localized modes in spatially periodic systems, we have put forward and analyzed a new optimization scheme for the construction of maximally localized Wannier functions. We analyzed bistable lasing and the switching dynamics in multimode photonic crystal microcavities, using analytical equation of motion techniques in a two-mode approximation as well as the numerically rigorous finite difference time domain (FDTD) method.

For homogeneously disordered random laser media, we have provided an answer to the long-standing problem of the origin of the finite-size lasing spots using a new transport theory for the spatial intensity correlations, coupling the

diffusive photon transport equations in the random medium self-consistently to the laser rate equations. In this way, we were able to predict the dependence of the average lasing spot size on the pump rate, which may be tested experimentally.

Finally, a diagrammatic perturbation theory was developed which allows to calculate physical quantities systematically to arbitrary order in the laser nonlinearity. While this theory is general, it is especially suitable for microlasers, where the field intensity varies usually on the scale of the wavelength of light, so that the laser nonlinearity induces strong renormalizations of physical quantities (like microcavity resonance frequencies) with respect to the passive system, which may cannot be treated in low order perturbation theory. We applied the theory first to the case of gas lasers, where strong resonance detuning may occur due to the Doppler shift of the atomic transition lines.

Acknowledgement This work was supported by the Deutsche Forschungsgemeinschaft through FOR 557.

References

1. K. Sakoda, *Optical Properties of Photonic Crystals* (Springer, Berlin, 2001)
2. M. Sargent III, M.O. Scully, W.E. Lamb Jr., *Laser Physics* (Addison-Wesley, Reading, 1974)
3. H. Haken, *Laser Theory* (Springer, Berlin, 1984)
4. D.M. Whittaker, M.P. Croucher, Phys. Rev. B **67**, 085204 (2003)
5. Y. Jiao, S. Mingaleev, M. Schillinger, D. Miller, S. Fan, K. Busch, IEEE Photonics Technol. Lett. **17**, 1875 (2005)
6. H. Takeda, A. Chutinan, S. John, Phys. Rev. B **74**, 195116 (2006)
7. T. Stollenwerk, D.N. Chigrin, J. Kroha, J. Opt. Soc. Am. B, Opt. Phys. **28**, 1951 (2011)
8. S.V. Zhukovsky, D.N. Chigrin, A.V. Lavrinenko, J. Kroha, Phys. Rev. Lett. **99**, 073902 (2007)
9. S.V. Zhukovsky, D.N. Chigrin, J. Kroha, Phys. Rev. A **79**, 033803 (2009)
10. D.N. Chigrin, S.V. Zhukovsky, A.V. Lavrinenko, J. Kroha, Phys. Status Solidi A **204**, 3647 (2007)
11. S.V. Zhukovsky, D.N. Chigrin, A.V. Lavrinenko, J. Kroha, Phys. Status Solidi B **244**, 1211 (2007)
12. S.V. Zhukovsky, D.N. Chigrin, Phys. Status Solidi B **244**, 3515 (2007)
13. S.V. Zhukovsky, D.N. Chigrin, A.V. Lavrinenko, J. Kroha, in *IEEE Lasers and Electro-Optics Society (LEOS)*, vol. 19 (2008), p. 2329
14. V.S. Letokhov, Sov. Phys. JETP **26**, 835 (1968)
15. P.W. Anderson, Phys. Rev. **109**, 1492 (1958)
16. K.L. van der Molen, P. Zijlstra, A. Lagendijk, A.P. Mosk, Opt. Lett. **31**, 1432 (2006)
17. R. Frank, A. Lubatsch, J. Kroha, J. Opt. A, Pure Appl. Opt. **11**, 114012 (2009)
18. R. Frank, A. Lubatsch, J. Kroha, Ann. Phys. **18**, 882 (2009)
19. L. Florescu, S. John, Phys. Rev. E **70**, 036607 (2004)
20. L.I. Deych, Phys. Rev. Lett. **95**, 043902 (2005)
21. L.I. Deych, in *Complex Media VI: Light and Complexity*, ed. by M.W. McCall, G. Dewar, M.A. Noginov (SPIE, Bellingham, 2005), p. 59240B
22. H.E. Türeci, A.D. Stone, B. Collier, Phys. Rev. A **74**, 043822 (2006)
23. H.E. Türeci, L. Ge, S. Rotter, A.D. Stone, Science **320**, 643 (2008)
24. O. Zaitsev, L. Deych, Phys. Rev. A **81**, 023822 (2010)
25. O. Zaitsev, J. Phys. B **43**, 245402 (2010)
26. C.A.J. Fletcher, *Computational Galerkin Methods* (Springer, Berlin, 1984)
27. C. Kremers, D.N. Chigrin, J. Kroha, Phys. Rev. A **79**, 013829 (2009)
28. C. Kremers, D.N. Chigrin, J. Opt. A, Pure Appl. Opt. **11**, 114008 (2009)
29. K.M. Leung, J. Opt. Soc. Am. B, Opt. Phys. **10**, 303 (1993)
30. E. Lidorikis, M.M. Sigalas, E.N. Economou, C.M. Soukoulis, Phys. Rev. Lett. **81**, 1405 (1998)
31. J. Albert, C. Jouanin, D. Cassagne, D. Bertho, Phys. Rev. B **61**, 4381 (2000)
32. J. Albert, C. Jouanin, D. Cassagne, D. Monge, Opt. Quantum Electron. **34**, 251 (2002)
33. N. Marzari, D. Vanderbilt, Phys. Rev. B **56**, 12847 (1997)
34. I. Souza, N. Marzari, D. Vanderbilt, Phys. Rev. B **65**, 035109 (2002)
35. A. Garcia-Martin, D. Hermann, F. Hagmann, K. Busch, P. Wölfle, Nanotechnology **14**, 177 (2003)
36. K. Busch, S. Mingaleev, A. Garcia-Martin, M. Schillinger, D. Hermann, J. Phys., Condens. Matter **15**, R1233 (2003)
37. E. Istrate, E.H. Sargent, Rev. Mod. Phys. **78**, 455 (2006)
38. A. McGurn, J. Phys. D, Appl. Phys. **38**, 2338 (2005)
39. J. des Cloizeaux, Phys. Rev. A **135**, 698 (1964)
40. K. Busch, S.F. Mingaleev, A. Garcia-Martin, M. Schillinger, D. Hermann, J. Phys., Condens. Matter **15**, R1233 (2003)
41. M. Mitchell, *An Introduction to Genetic Algorithms* (MIT Press, Cambridge, 1999)
42. K.J. Vahala, Nature **424**, 839 (2003)
43. K. Yoshino, Y. Shimoda, Y. Kawagishi, K. Nakayama, M. Ozaki, Appl. Phys. Lett. **75**, 932 (1999)
44. S. Mahnkopf, M. Kamp, A. Forchel, R. März, Appl. Phys. Lett. **82**, 2942 (2003)
45. W. Park, J.-B. Lee, Appl. Phys. Lett. **85**, 4845 (2004)
46. E. Schonbrun, M. Tinker, W. Park, J.-B. Lee, IEEE Photonics Technol. Lett. **17**, 1196 (2005)
47. A. Figotin, Y.A. Godin, I. Vitebsky, Phys. Rev. B **57**, 2841 (1998)
48. H. Yu, B. Tang, J. Li, L. Li, Opt. Express **13**, 7243 (2005)
49. E.P. Kosmidou, E.E. Kriezis, T.D. Tsiboukis, IEEE J. Quantum Electron. **41**, 657 (2005)
50. A. Siegman, *Lasers* (University Science Books, Mill Valley, 1986)
51. W. Lee, W.R. Lempert, Appl. Opt. **42**, 4320 (2003)
52. S.E. Hodges, M. Munroe, J. Cooper, M.G. Raymer, J. Opt. Soc. Am. B **14**, 191 (1997)
53. L. Florescu, K. Busch, S. John, J. Opt. Soc. Am. B **19**, 2215 (2002)
54. M.M. Dignam, D.P. Fussell, M.J. Steel, R.C. McPhedran, C.M. de Sterke, Phys. Rev. Lett. **96**, 103902 (2006)
55. D.P. Fussell, M.M. Dignam, M.J. Steel, C.M. de Sterke, R.C. McPhedran, Phys. Rev. A **74**, 043806 (2006)
56. M. Tokushima, H. Yamada, Y. Arakawa, Appl. Phys. Lett. **84**, 4298 (2004)
57. S.H.G. Teo, A.Q. Liu, C. Lu, J. Singh, M.B. Yu, Photonics Nanostruct. Fundam. Appl. **4**, 103 (2006)
58. G.P. Agrawal, N.K. Dutta, J. Appl. Phys. **56**, 664 (1985)
59. S. Ishii, T. Baba, Appl. Phys. Lett. **87**, 181102 (2005)
60. J. Bang, K. Blotekjar, R. Ellingsen, IEEE J. Quantum Electron. **27**, 2356 (1991)
61. A.S. Nagra, R.A. York, IEEE Trans. Antennas Propag. **46**, 334 (1998)
62. X. Jiang, C.M. Soukoulis, Phys. Rev. Lett. **85**, 70 (2000)
63. S.-H. Chang, A. Taflove, Opt. Express **12**, 3827 (2004)
64. P. Bermel, A. Rodriguez, S.G. Johonson, J.D. Joannopoulos, M. Soljacic, Phys. Rev. A **74**, 043818 (2006)

65. S.V. Zhukovsky, D.N. Chigrin, A.V. Lavrinenko, J. Kroha, Phys. Status Solidi B **244**, 1211 (2006)
66. G.M. Slavcheva, J.M. Arnold, R.W. Ziolkowski, IEEE J. Quantum Electron. **10**, 1052 (2004)
67. M.-K. Seo, G. Song, I.-K. Hwang, Y.-H. Lee, Opt. Express **13**, 9645 (2005)
68. A. Lavrinenko, P. Borel, L. Frandsen, M. Thorhauge, A. Harpøth, M. Kristensen, T. Niemi, H. Chong, Opt. Express **12**, 234 (2004)
69. O.A. Lavrova, D.J. Blumenthal, J. Lightwave Technol. **18**, 1274 (2000)
70. N.M. Lawandy, R.M. Balachandran, A.S.L. Gomes, E. Sauvain, Nature **368**, 436 (1994)
71. H. Cao, Y.G. Zhao, H.C. Ong, S.T. Ho, J.Y. Dai, J. Wu, R.P.H. Chang, Appl. Phys. Lett. **73**, 3656 (1998)
72. H. Cao, Y.G. Zhao, S.T. Ho, E.W. Seelig, Q.H. Wang, R.P.H. Chang, Phys. Rev. Lett. **82**, 2278 (1999)
73. H. Cao, Waves Random Complex Media **13**, R1 (2003)
74. S. Gottardo, S. Cavalieri, O. Yaroshchuk, D.A. Wiersma, Phys. Rev. Lett. **93**, 263901 (2004)
75. V.M. Markushev, V.F. Zolin, C.M. Briskina, Zh. Prikl. Spektrosk. **45**, 84 (1986)
76. M. Bahoura, K.J. Morris, M.A. Noginov, Opt. Commun. **201**, 405 (2002)
77. S. Klein, O. Cregut, D. Gindre, A. Boeglin, K.D. Dorkeno, Opt. Express **3**, 5387 (2005)
78. R.C. Polson, Z.V. Vardeny, Appl. Phys. Lett. **85**, 1289 (2004)
79. H. Cao, J.Y. Xu, D.Z. Zhang, S.H. Chang, S.T. Ho, E.W. Seelig, X. Liu, R.P.H. Chang, Phys. Rev. Lett. **84**, 5584 (2000)
80. H. Cao, Y. Ling, J.Y. Xu, C.Q. Cao, P. Kumar, Phys. Rev. Lett. **86**, 4524 (2001)
81. V.M. Apalkov, M.E. Raikh, B. Shapiro, Phys. Rev. Lett. **89**, 016802 (2002)
82. C. Vanneste, P. Sebbah, H. Cao, Phys. Rev. Lett. **89**, 016802 (2007)
83. A. Lubatsch, J. Kroha, K. Busch, Phys. Rev. B **71**, 184201 (2005)
84. R. Frank, A. Lubatsch, J. Kroha, Phys. Rev. B **73**, 245107 (2006)
85. R. Frank, A. Lubatsch, Phys. Rev. A **84**, 013814 (2011)
86. T.S. Misirpashaev, C.W.J. Beenakker, Phys. Rev. A **57**, 2041 (1998)
87. G. Hackenbroich, J. Phys. A **38**, 10537 (2005)
88. O. Zaitsev, L.I. Deych, V. Shuvayev, Phys. Rev. Lett. **102**, 043906 (2009)
89. W.E. Lamb Jr., Phys. Rev. **134**, 1429 (1964)